



The impact of microlensing on the standardization of strongly lensed Type Ia supernovae

Max Foxley-Marrable,¹ Thomas E. Collett,¹ Georgios Vernardos,^{2,3}
Daniel A. Goldstein^{4,5} and David Bacon¹

¹Institute of Cosmology and Gravitation, University of Portsmouth, Dennis Sciama Building, Burnaby Road, Portsmouth, PO1 3FX, UK

²Kapteyn Astronomical Institute, University of Groningen, P.O. Box 800, NL-9700 AV Groningen, the Netherlands

³Centre for Astrophysics & Supercomputing, Swinburne University of Technology, PO Box 218, Hawthorn, Victoria, 3122, Australia

⁴Department of Astronomy, University of California, Berkeley, CA 94720, USA

⁵Lawrence Berkeley National Laboratory, Berkeley, CA 94720, USA

Accepted 2018 May 17. Received 2018 May 2; in original form 2018 February 21

ABSTRACT

We investigate the effect of microlensing on the standardization of strongly lensed Type Ia supernovae (GLSNe Ia). We present predictions for the amount of scatter induced by microlensing across a range of plausible strong lens macromodels. We find that lensed images in regions of low convergence, shear and stellar density are standardizable, where the microlensing scatter is $\lesssim 0.15$ mag, comparable to the intrinsic dispersion of a typical SN Ia. These standardizable configurations correspond to asymmetric lenses with an image located far outside the Einstein radius of the lens. Symmetric and small Einstein radius lenses ($\gtrsim 0.5$ arcsec) are not standardizable. We apply our model to the recently discovered GLSN Ia iPTF16geu and find that the large discrepancy between the observed flux and the macromodel predictions from More et al. cannot be explained by microlensing alone. Using the mock GLSNe Ia catalogue of Goldstein et al., we predict that ~ 22 per cent of GLSNe Ia discovered by Large Synoptic Survey Telescope (LSST) will be standardizable, with a median Einstein radius of 0.9 arcsec and a median time delay of 41 d. By breaking the mass-sheet degeneracy the full LSST GLSNe Ia sample will be able to detect systematics in H_0 at the 0.5 per cent level.

Key words: gravitational lensing: strong – gravitational lensing: micro – supernovae: general – supernovae: individual: iPTF16geu – cosmological parameters – cosmology: observations.

1 INTRODUCTION

The value of the Hubble constant H_0 is a major point of contention in cosmology today, bringing the validity of the Lambda-Cold Dark Matter (Λ CDM) model of cosmology into question. This particularly arises from the 3.4σ tension between the Planck Collaboration et al. (2016) result of $H_0 = 67.8 \pm 0.9 \text{ km s}^{-1} \text{ Mpc}^{-1}$, derived from the cosmic microwave background (CMB), and the Riess et al. (2016) result of $H_0 = 73.2 \pm 1.7 \text{ km s}^{-1} \text{ Mpc}^{-1}$, measured from low-redshift supernovae and Cepheids. The Planck Collaboration et al. (2016) result infers H_0 assuming Λ CDM, whilst the Riess et al. (2016) result probes H_0 directly. Whilst this tension could be attributed to statistical fluke or unaccounted systematics, it potentially signals new physics beyond the Λ CDM model. Hence the

need for precise and independent measurements of H_0 is greater than ever, such that the validity of the Λ CDM model can be tested.

Strong gravitational lenses are powerful probes of cosmology (Oguri et al. 2012; Suyu et al. 2013; Collett & Auger 2014) and are particularly sensitive to H_0 through time delay cosmography (Treu & Marshall 2016). The light from each image in a lensing system takes a different path through the lens before reaching the observer. If the lensed object is a variable source, the images vary asynchronously with a geometrical time delay based on these path differences. Time delays have an additional component caused by the gravitational potential of the lens (Shapiro 1964). When a background source peaks sharply in luminosity, the time delay between each image can in principle be measured by observing the time difference between the peaks of each image.

Time delays allow strong gravitational lenses to measure H_0 independently of assumptions made in the cosmological model: the value of H_0 is mostly invariant to other cosmological parameters such as the curvature and the dark energy equation of state (Bonvin

* E-mail: max.foxley-marrable@port.ac.uk

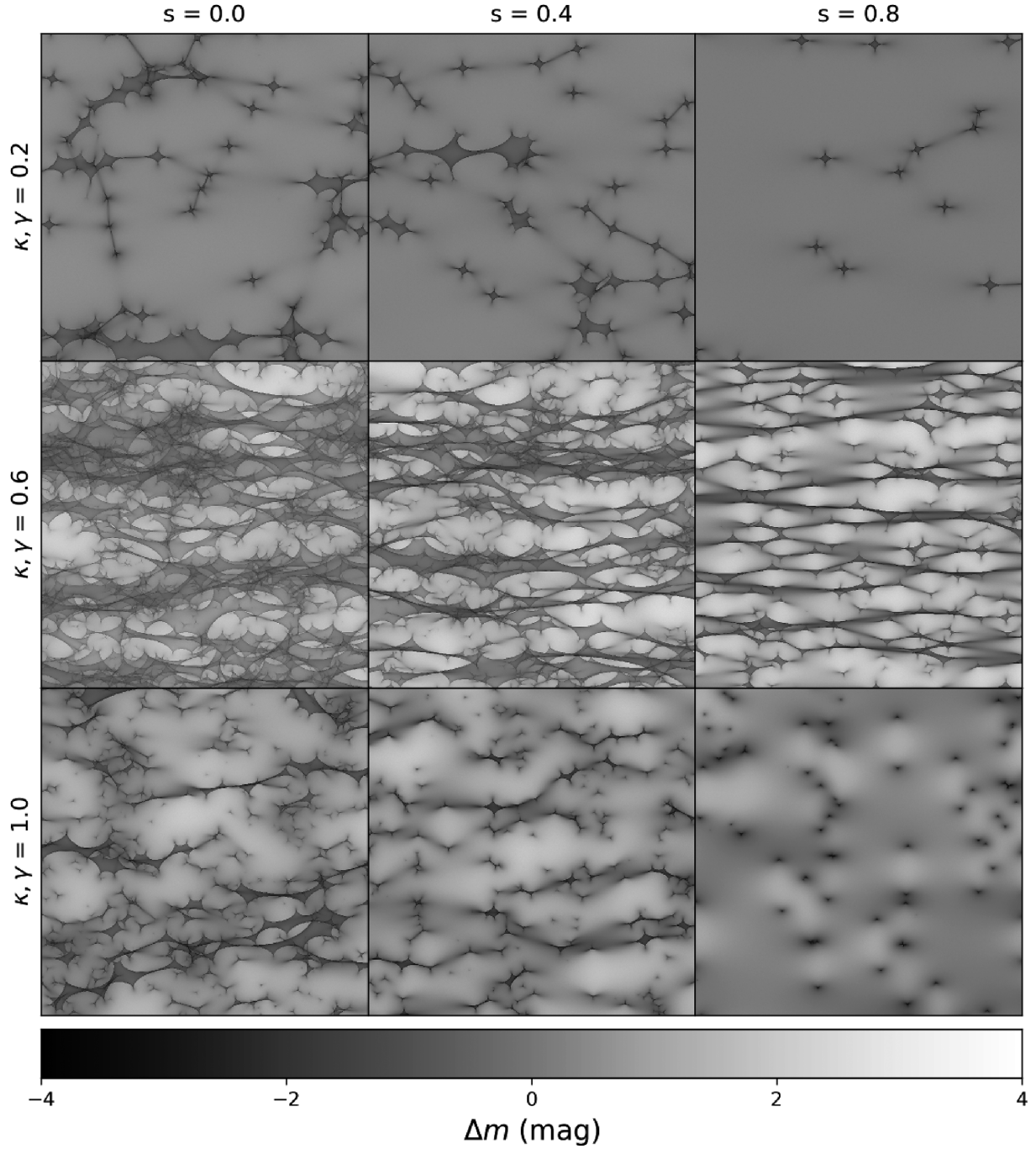


Figure 1. Example of microlensing maps corresponding to various combinations of the convergence κ , shear γ , and smooth (dark) matter fraction s . Each side in a subpanel spans a physical range of $13.7 R_{\text{Ein}, \odot} = 5 \times 10^{12}$ km. The maps show microlensing caustics projected on to the source plane as a result of inverse ray-tracing through a foreground star field. The colour scale represents the deviation in magnitudes from the smooth macromodel magnification.

et al. 2017). The most recent example is Bonvin et al. (2017), which used time delays from three lensed quasars to independently measure $H_0 = 71.9^{+2.4}_{-3.0}$ km s $^{-1}$ Mpc $^{-1}$ to within a 3.8 per cent precision. In order to obtain a value for H_0 through strong lens time delays, one needs to know the 2D lens potential and the unlensed source position, neither of which can be observed directly. The use of lens modelling is therefore required in order to infer these quantities.

However, strong lens models are subject to degeneracies, which are a major source of uncertainty for time delay cosmography (Schneider & Sluse 2014). The main component of the degener-

acy is the mass-sheet degeneracy: when rescaling the mass of the lens with an additional sheet of mass of constant density, the image configurations remain exactly the same but the projected mass on each image (also known as the convergence κ) changes, affecting the time delay (Falco, Gorenstein & Shapiro 1985). Put simply, two lens models producing identical image configurations can have very different time delays. Breaking the mass-sheet degeneracy is therefore necessary to constrain H_0 . In order to break the mass-sheet degeneracy additional information is required, such as the intrinsic luminosity of the background source (Kolatt & Bartelmann 1998).

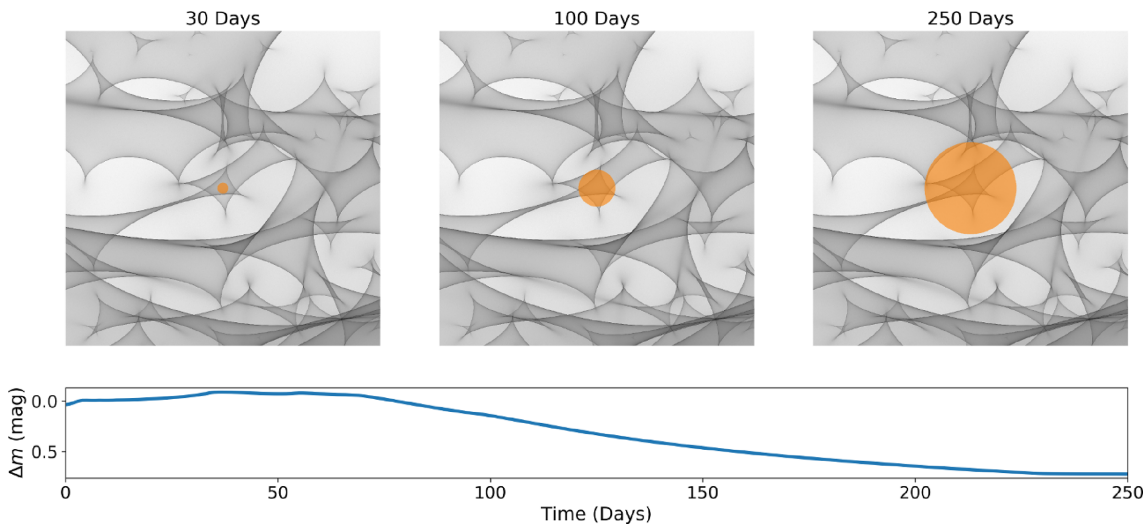


Figure 2. A zoomed in microlensing map (each side corresponding to $2.75 R_{\text{Ein}, \odot} = 1 \times 10^{12}$ km) with a SN Ia profile superimposed on top, expanding at a rate of $2.5 \times 10^{-8} R_{\text{Ein}, \odot} \text{ s}^{-1} = 10^4 \text{ km s}^{-1}$. At each time-step, the SN Ia profile is convolved with the microlensing background: the magnifications inside the disc are summed up and averaged. As the SN Ia profile grows, it crosses more and caustics, causing the microlensing magnification to vary over time. The resulting magnifications are shown in the bottom panel.

Originally proposed by Refsdal (1964), the prospect of using strongly lensed supernovae (GLSNe) to precisely measure H_0 is promising, especially after the discovery of the Type Ia GLSN iPTF16geu in 2016 October (Goobar et al. 2017). The light curves of Type Ia Supernovae (SNe Ia) are standardizable (Phillips 1993), allowing us to infer their intrinsic luminosity. Hence, GLSNe Ia can potentially lift the mass-sheet degeneracy (Oguri & Kawano 2003) and enable a test of systematic uncertainties in time delay cosmography.

GLSNe are advantageous over the lensed active galactic nuclei (AGN) currently used for time delay cosmography (Vuissoz et al. 2008; Suyu & Halkola 2010; Tewes et al. 2013; Bonvin et al. 2016). SN light curves have a strong peak before they decay, occurring over a time-scale of several weeks, whilst AGN light curves vary stochastically and heterogeneously, with weak variations in luminosity. Hence GLSN time delays can be obtained in a single observing season, whilst AGN must be monitored over several years in order to acquire accurate time delays (Liao et al. 2015).

Goldstein et al. (2018) predicts that ~ 930 GLSNe Ia will be discovered by the Large Synoptic Survey Telescope (LSST) (LSST Science Collaboration et al. 2009) over its 10 yr survey, with 70 per cent of the GLSNe Ia having time delays that can be measured precisely.

Despite the potential power of GLSNe Ia, there exists one major theoretical barrier to their use as cosmological probes: microlensing caused by stars in the foreground lensing galaxy. Microlensing can independently magnify or demagnify individual images of the background source (Bagherpour, Branch & Kantowski 2006; Dobler & Keeton 2006), introducing scatter into the shape and amplitude of the resulting light curves. The effect of microlensing on each lensed image can be inferred by obtaining its convergence κ ,¹ shear γ , and smooth matter fraction s through lens modelling. κ and γ represents the amount of mass projected on and near the image, respectively, while s represents the projected fraction of mass in dark matter as opposed to stellar matter (see Fig. 1). Due to the distribution and random motion of the stars in the foreground

galaxy, inferring the effect of microlensing on one image does not infer the effect of microlensing on the other image(s). This can significantly reduce the reliability of any time delay and luminosity measurement, as microlensing can randomly distort the light curve of each image, such that the intrinsic magnification and luminosity of the source can be difficult to determine. This effect also evolves over time. As the background SN Ia grows, the number of microlensing caustics that its light profile intersects with increases with time (see Fig. 2). Recently, Goldstein et al. (2018) have shown that time delays can be robustly measured using early time colour curves.

More et al. (2017) modelled iPTF16geu using the GLAFIC (Oguri 2010) and GLEE (Suyu & Halkola 2010; Suyu et al. 2012) macro lens models. Whilst the models themselves were in agreement, they were in contention with the Goobar et al. (2017) observations, with a discrepancy of almost 2 mag for the brightest image. Their conclusion was that the disparity between their lens models and the observations was primarily due to microlensing from foreground stars in the lensing galaxy.²

In this paper, we examine the effect microlensing has on an expanding SN Ia profile across a wide range of image configurations corresponding to particular values of κ , γ , and s . We provide the first predictions for regions of parameter space where the SN Ia image has a standardizable light curve, allowing us to infer its intrinsic luminosity and hence break the mass-sheet degeneracy. We define a standardizable supernova as one where the scatter due to microlensing is less than 0.15 mag, comparable to the intrinsic dispersion of an unlensed SN Ia after standardization (Betoule et al. 2014; Macaulay et al. 2017). We also present predictions for the fraction of GLSNe Ia discovered by LSST that will be standardizable. Finally we analyse the effect of microlensing on iPTF16geu and compare our results against the More et al. (2017) prediction. In Section 2 we describe our microlensing simulations. In Section 3 we present and discuss our subsequent analysis with results and

¹ κ is composed of both stellar and dark matter components.

²More et al. (2017) also mention the possibility of milli-lensing.

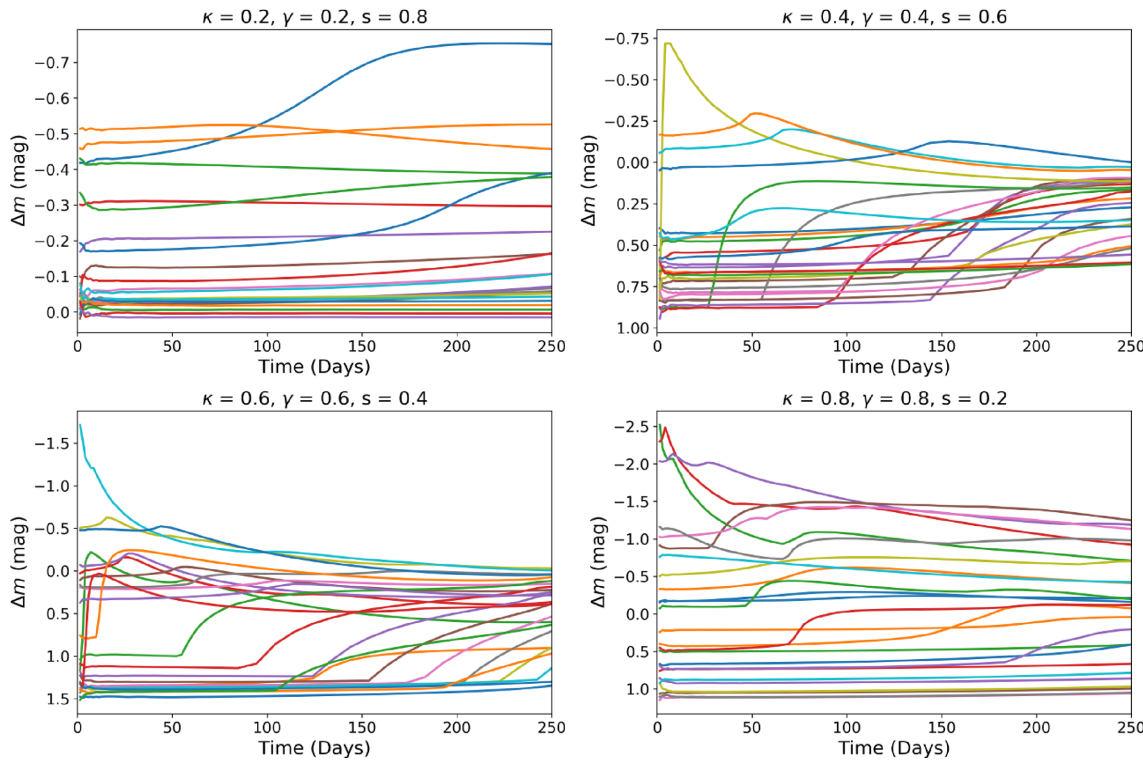


Figure 3. A selection of simulated microlensing light curves for an expanding uniform disc. The four panels correspond to different values of the convergence κ , shear γ , and smooth matter fraction s . Each light curve within a panel has the same macrolensing parameters but a different realization of the microlensing by stars.

conclude in Section 4. Throughout this paper we report results in the observer time frame assuming a source redshift of 0.409.

2 SIMULATIONS

To simulate the effect of microlensing by stars in the lens galaxy, we use magnification maps generated by the GERLUMPH project³ as shown in Fig. 1 (Vernardos et al. 2014; Vernardos & Fluke 2014). These are pixelated maps of the source plane where the magnification per pixel has been calculated using the inverse ray-shooting technique (Kayser, Refsdal & Stabell 1986). A field of randomly distributed point masses is used to simulate the star field, with each star having the same mass. The deflections for each microlens are computed directly and in parallel using the graphics processing unit (GPU) implementation of Thompson et al. (2010, 2014).

Each magnification map used in this work is square with 10 000 pixels on a side, with a side corresponding to $13.7 R_{\text{Ein}, \odot}$. $R_{\text{Ein}, \odot}$ is the Einstein radius for a $1 M_\odot$ microlens; for a lens at $z_l = 0.216$ and a source at $z_s = 0.409$. This corresponds to a physical scale of $R_{\text{Ein}, \odot} = 4 \times 10^{11} \text{ km} = 2 \times 10^{-6} \text{ arcsec}$ on the sky, with each map pixel covering an area of $2.5 \times 10^{17} \text{ km}^2 = 9 \times 10^{-18} \text{ arcsec}^2$ on the sky.⁴

To sample a wide range of possible GLSN configurations we use the GD1 set of maps (described in detail in Vernardos et al. 2014). This set covers κ, γ space on a uniform grid with $\Delta\kappa, \Delta\gamma = 0.05$,

and $0 \lesssim \kappa, \gamma \lesssim 1.7$. For each κ, γ combination there are 11 values of s available: $0 \leq s \leq 0.9$, in steps of 0.1, and $s = 0.99$. For each κ, γ pair we use maps with a smooth matter fraction $s = 0.2, 0.4, 0.6, 0.8$. This results in a total of 4488 magnification maps.

To obtain the SN microlensing light curves we convolve the magnification maps with a time varying profile of the background source (see Fig. 2). We use an expanding uniform disc to approximate the SN brightness profile. This simple model is sufficient for our purposes since the observed luminosity of a microlensed source is mostly sensitive to the average size and largely independent of any specific shape of the source profile (Mortonson, Schechter & Wambsganss 2005). We do not consider sources with clumpy profiles.

The supernova expansion rate is set to $10^4 \text{ km s}^{-1} = 2.5 \times 10^{-8} R_{\text{Ein}, \odot} \text{ s}^{-1}$. Since this is much larger than any of the velocities involved (i.e. the peculiar velocity of the lens and the source, the velocity of the observer, and the proper motions of the microlenses), we can approximate the microlensing map as time invariant, and the centroid of a supernova as constant; only the radius of the supernova changes with time. At this expansion rate we are able to place 10^4 SNe per magnification map without profile overlap within the first 60 d.

To obtain a light curve for an individual SN, we choose a position on the magnification map, and evaluate the product of its profile and the magnification map at each time-step. This is done for a total of 55 time-steps: $0 < t < 16 \text{ d}$ with $\delta t = 1 \text{ d}$, $16 < t < 60 \text{ d}$ with $\delta t = 2 \text{ d}$, and $60 < t < 200 \text{ d}$ with $\delta t = 7 \text{ d}$. A total of $\approx 250 000$ convolutions between maps and profiles have been performed, requiring roughly 300 GPU h.

We normalize all of our unlensed source fluxes to unity at all times, such that our light curves depend only on the mi-

³<http://gerlumph.swin.edu.au>

⁴Here we assume the best-fitting Λ CDM cosmological parameters of Planck Collaboration et al. (2016).

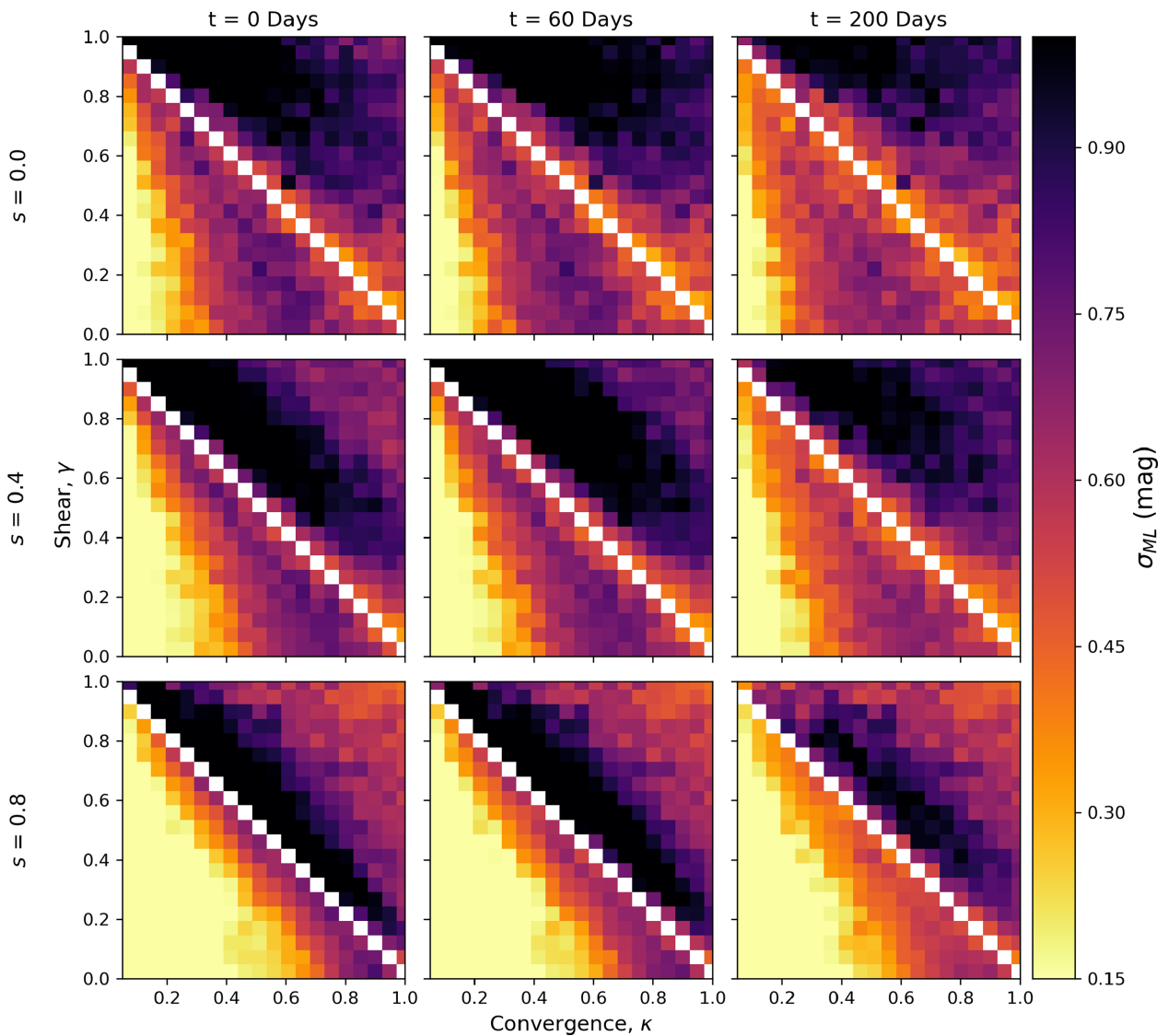


Figure 4. The microlensing scatter in the observed luminosity of a lensed supernova image. Each subpanel shows the scatter as a function of the convergence κ and shear γ at fixed smooth matter fraction s and time t after explosion. The smooth matter fraction increases from top to bottom and the time of observation increases from left to right. The white pixels along the diagonal correspond to regions of infinite magnification: lensed images do not form here.

croclensing rather than intrinsic variations in the unlensed source. We show a range of examples of microlensing light curves in Fig. 3.

3 RESULTS AND DISCUSSION

3.1 Microlensing scatter

For each $\kappa-\gamma$ pair, time-step, and value of the smooth matter fraction s , we measured the scatter by taking half the difference of the 16th and 84th percentile of the resulting probability density function (PDF).⁵

In Fig. 4, we show how the microlensing scatter σ_{ML} varies with κ , γ , and s , across a range of times t . We find that there is a region

of parameter space where the light curves from GLSNe Ia are standardizable as the scatter due to microlensing is comparable to the typical intrinsic dispersion for a SN Ia after standardization (Betoule et al. 2014; Macaulay et al. 2017). Therefore, with the correct lensing configuration, it is possible to infer the unlensed magnitude of the source SN Ia. This will lift the mass-sheet degeneracy and allow us to acquire an accurate, precise, and independent measurement of the Hubble Constant H_0 .

We find that the standardizable region corresponds to lensed images with low κ and γ , with the size of the standardizable region increasing with s , i.e. images forming in regions of lower stellar density are less susceptible to microlensing. Physically, this corresponds to a lens with an asymmetric image configuration, with at least one image located far outside the Einstein radius of the lens. This outermost image experiences the least amount of microlensing due to being far away from the high-stellar density region of the lensing galaxy and hence could be used to infer the unlensed magnitude of the background SN Ia.

⁵Equivalent to calculating a 1σ standard deviation for a Gaussian distribution.

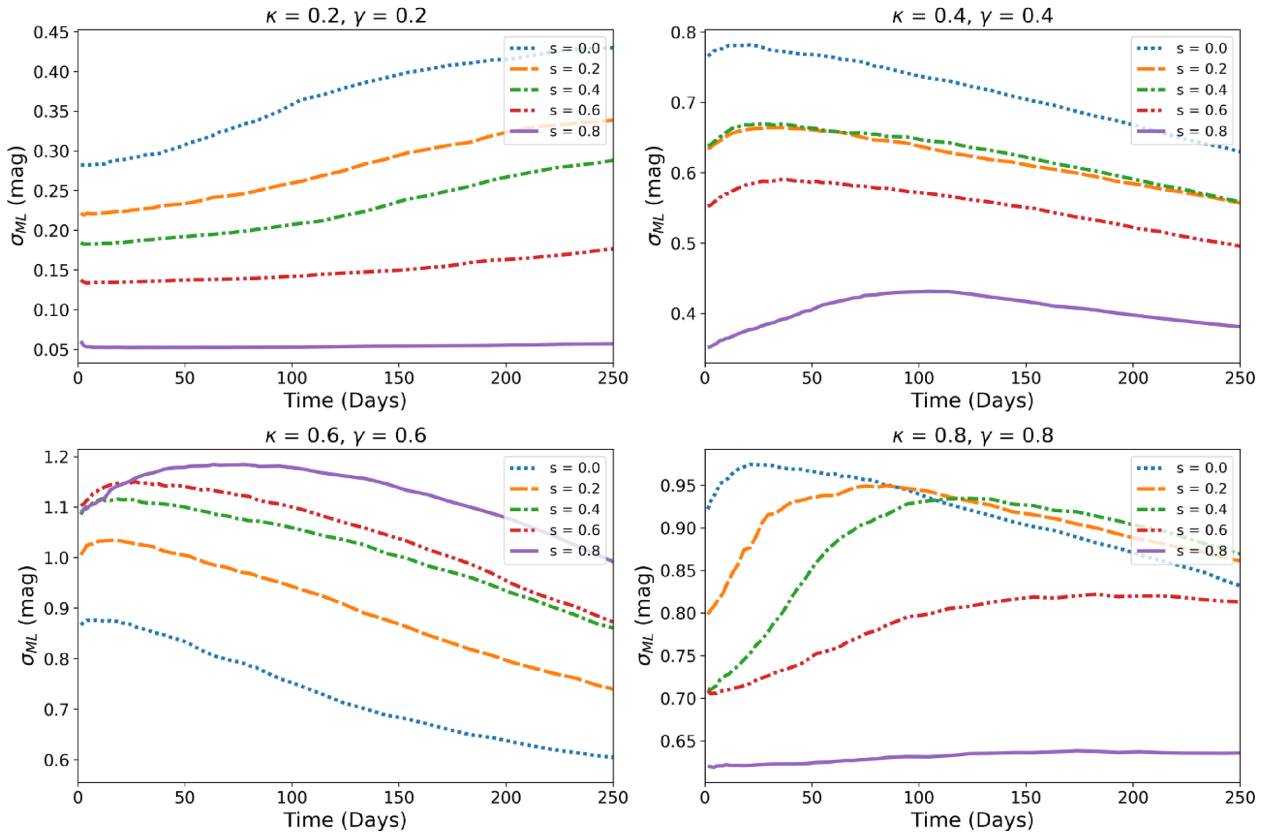


Figure 5. The microlensing induced scatter in the observed luminosity as a function of time. The different lines correspond to different values of the smooth matter fraction s .

As highlighted in Fig. 5, the microlensing scatter in low κ, γ regions increases over time, meaning early time measurements of the SN image fluxes are optimal for cosmography. This counter-intuitive result is because there are few caustics in these situations and a small source will typically fall in the smooth region between caustics (see Fig. 1). A small number of systems will be highly magnified but these are excluded by our choice to define width as half the 68 per cent confidence region. As the source expands it is more likely to cross a caustic, creating a larger spread of magnifications at late time. The scatter does not decrease at late times as the source is still too small to average over many caustics. However, in higher κ, γ regions, the scatter decreases with time and increases with s . This behaviour is due to the increased density of microlensing caustics. As the source expands it averages over more caustics and the scatter shrinks, but this still does not reach a standardizable level even after 200 d.

3.2 How many lensed supernovae are standardizable?

To investigate the fraction of lensed supernovae that will be standardizable, we first use a simple lens model to relate lensed image position to the expected microlensing scatter. We assume a singular isothermal sphere (SIS) lens model and iPTF16geu redshifts of $z_l = 0.216$ and $z_s = 0.409$ for the lens and source, respectively.

For each point on the image plane, κ and γ can be inferred from the macro lens model, however, the macro model is sensitive only to the total mass and not the partition between stars and dark matter. The smooth matter fraction is given by the fraction of the surface

density not in stars

$$s = 1 - \frac{\kappa_*}{\kappa_{\text{tot}}}. \quad (1)$$

The total mass distribution is modelled using an SIS lens profile

$$\kappa_{\text{tot}} = \kappa_{\text{SIS}} = \frac{R_{\text{Ein}}}{2r}, \quad (2)$$

where r denotes a position in the image plane in polar coordinates. For the stellar component of equation (1) we assume a de Vaucouleurs profile

$$\kappa_* = \kappa_{\text{dev}}(r) = Ae^{-k(r/R_e)^{1/4}}, \quad (3)$$

where A is a normalization constant, R_e is the effective radius of the lens and $k = 7.669$ (Dobler & Keeton 2006). To calculate the normalization constant A , we match the dark matter fractions to those found in typical strong lensing ellipticals in the Sloan Lens ACS (SLACS) sample (Auger et al. 2010)

$$A = (1 - f_{\text{DM}}) \frac{M_{\text{tot}}}{M_*}, \quad (4)$$

where M_{tot} and M_* were inferred by integrating equations (2) and (3) in polar coordinates from 0 to $R_e/2$. f_{DM} is the total projected fraction of dark matter within half the effective radius of the galaxy. Our f_{DM} is then matched to the fit derived in Auger et al. (2010)

$$f_{\text{DM}} = a \times \log(\sigma_{R_e/2}) + b, \quad (5)$$

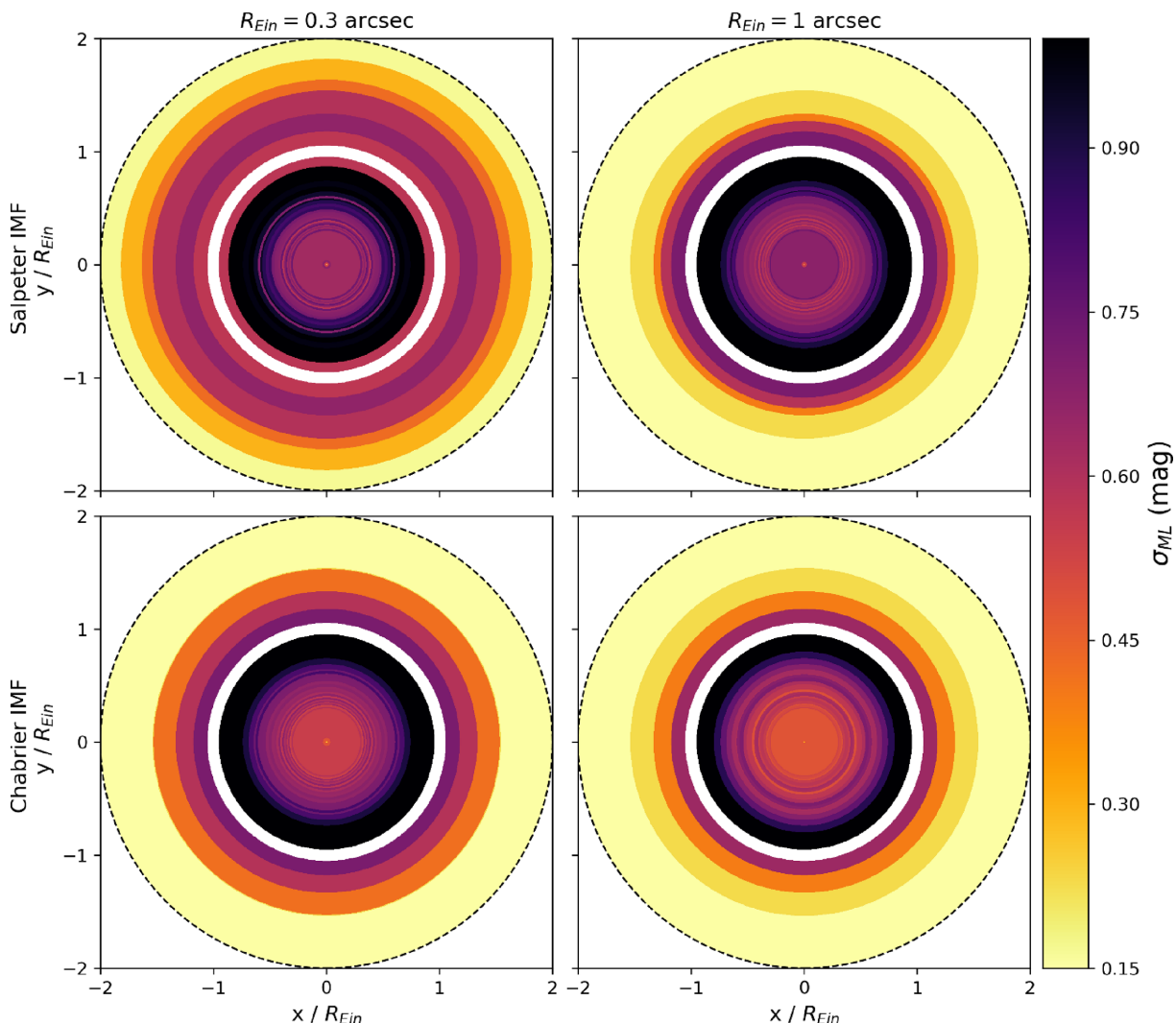


Figure 6. The amount of microlensing scatter induced on any lensed image at any point on the image plane, assuming an SIS lens and an SN 30 d after explosion. The four panels show the effect of varying the Einstein Radii, R_{Ein} , and the IMFs. The black dashed line represents the outermost boundary for multiple imaging. The inner white circle corresponds to the critical curve and infinite magnification. The Salpeter and Chabrier IMFs correspond to the dark matter fractions derived in Auger et al. (2010).

where a and b are fitting parameters that depend on the initial mass function (IMF) of the lens and $\sigma_{R_{e/2}}^6$ is the velocity dispersion within half the effective radius of the lens (Auger et al. 2010). Assuming a Salpeter IMF, $a = 0.80 \pm 0.44$ and $b = 0.05 \pm 0.18$ while for a Chabrier IMF, $a = 0.46 \pm 0.22$ and $b = 0.40 \pm 0.09$ (Auger et al. 2010).

Using our model for κ , γ , and s across the image plane and the results of Section 3.1, we determine the microlensing scatter as a function of GLSN image plane position. This is shown in Fig. 6, which shows that standardizable images form beyond the Einstein radius corresponding to an asymmetric configuration. More of the image plane is standardizable if the Einstein radius is large or if the IMF is Chabrier rather than Salpeter. The Chabrier IMF has a lower mass-to-light ratio, so places a larger fraction of the total mass in dark matter whereas the Salpeter IMF places more mass in low-mass stars.

⁶In units of 100 km s^{-1} .

In order to infer how often standardizable images form, we must determine the fraction of the source plane that is standardizable. We solve the lens equation for a range of source positions and Einstein radii. For each source position we infer the microlensing scatter for all images formed. Fig. 7 shows the fraction of the source plane that is standardizable as a function of R_{Ein} , for an SN 30 d after explosion, assuming either a Salpeter or Chabrier IMF. For a Salpeter IMF ~ 70 per cent of the source plane is standardizable provided $R_{Ein} \gtrsim 1$ arcsec on the sky. Decreasing R_{Ein} causes the standardizable fraction of the source plane to sharply decline to zero at $R_{Ein} \sim 0.5$ arcsec. More of the source plane is standardizable if the IMF is Chabrier: lenses as small as $R_{Ein} \sim 0.4$ arcsec can have a source plane which is 70 per cent standardizable, but sharply dropping to 0 per cent at $R_{Ein} \sim 0.2$ arcsec.

In principle, measuring the scatter for a sample of GLSNe Ia with $R_{Ein} \sim 0.5$ arcsec will allow us to discriminate between IMFs in the lensing galaxy. If the Auger et al. (2010) Salpeter fit is correct then no lensed SNe with $R_{Ein} < 0.5$ arcsec should have a scatter of less

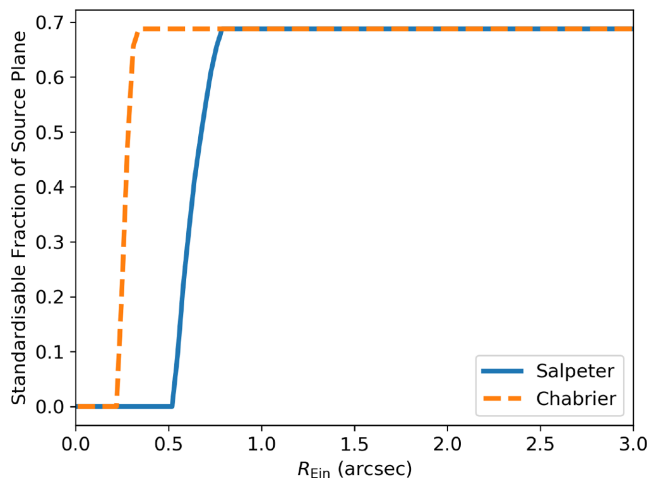


Figure 7. The percentage of the source plane that is standardizable as a function of the Einstein radius R_{Ein} of the lens 30 d after explosion. The result is sensitive to the dark matter fraction in the lens: the solid blue and dashed orange lines correspond to the dark matter fractions derived in Auger et al. (2010) for a Salpeter and Chabrier IMF, respectively.

than 0.15 mags whilst most lensed SNe will if the Chabrier fit is correct.

The above toy model neglects magnification bias. Whilst asymmetric configurations dominate the source plane, they are less highly magnified and therefore harder to detect than more symmetric configurations. To illustrate this we take the mock GLSNe catalogue of Goldstein et al. (2018) and assess the standardizable fraction of systems where the brightest SN image reaches a peak apparent i -band magnitude of 22.15. This choice roughly approximates the LSST discovery threshold for GLSNe. We predict that 22 per cent of the ~ 930 GLSNe Ia to be discovered by LSST will be standardizable, of which approximately 1 in 5 will be quads. The median time delay for a standardizable LSST GLSN Ia is 44 d, compared to 18 d for all LSST GLSN Ia. The median Einstein radius for a standardizable LSST GLSN Ia is 0.9 arcsec, compared to 0.7 arcsec for all LSST GLSN Ia. The catalogue spans a range of Einstein radii between $0.06 \text{ arcsec} \leq R_{\text{Ein}} \leq 2.54 \text{ arcsec}$.

3.3 Lifting the mass-sheet degeneracy with LSST GLSNe Ia: predictions for H_0

The fundamental gain of a GLSNe Ia over a standard time delay lens is the ability to test for the presence of systematic uncertainties in the lens model. Since lens models have typical errors of a few percent (Wong et al. 2017), a 0.15 mag uncertainty on the flux of a single lensed image will not provide statistically relevant improvement on H_0 . Averaging over many lensed supernovae will be required to constrain H_0 with interesting accuracy.

To investigate the expected constraints on H_0 from the final LSST GLSNe Ia sample, we draw 650 GLSNe Ia from our mock LSST catalogue. This is the number of GLSNe Ia forecast to be discovered by LSST early enough to measure reliable time delays (Goldstein et al. 2018). Taking a typical 7 per cent error per system (Bonvin et al. 2017) and scaling by root N, gives $\sigma_{H_0} = 0.3$ per cent, however, this neglects residual systematics from the mass-sheet degeneracy.

Given the individual magnification probability $P(\mu)$ for each image of a GLSN, the expected PDF for the unlensed magnitude of

Table 1. Table of parameters used for iPTF16geu simulations. κ and γ were taken from More et al. (2017). Values of the smooth matter fraction s were inferred from our lens model of iPTF16geu.

Image	κ	γ	s
A	0.56	0.56	0.22
B	0.43	0.43	0.23
C	0.57	0.56	0.27
D	0.46	0.45	0.23

the supernova is given by

$$P(M_{\text{SN}}) = \prod_{\forall i} P(\mu_i). \quad (6)$$

Adding this in quadrature to an intrinsic SN Ia scatter of 0.1 mag (Betoule et al. 2014), gives the expected uncertainty on the macro-model magnifications for the lens.

Constraining the true macromodel magnifications gives constraints on the mass-sheet degeneracy parameter λ , since

$$\mu_{\text{True}} = \mu_{\text{Model}}/\lambda^2, \quad (7)$$

where μ_{True} is the true magnification and μ_{Model} is the macromodel magnification assuming $\lambda = 0$. This implies that a system with a microlensing scatter of 0.15 mag gives a constraint on λ with 17 per cent precision that is insensitive to the mass-sheet transformation.

The time delays – and hence $1/H_0$ – are proportional to λ . The product of $P(\lambda)$ over all the systems gives the level at which the mass-sheet degeneracy can be broken for the final constraint on H_0 . This product has a width of $\sigma_\lambda = 0.5$ per cent. Combined, the 650 LSST GLSNe Ia will therefore be able to detect systematics in H_0 due to the mass-sheet transformation at the 0.5 per cent level. If we restrict the sample to the 140 GLSNe with a microlensing scatter of less than 0.15 mag, the constraints on H_0 degrade to $\sigma_{H_0} = 0.6$ per cent. If only the 44 standardizable quad image systems are used, the constraints H_0 degrade to $\sigma_{H_0} = 1.1$ per cent.

3.4 iPTF16geu

The recent observations of iPTF16geu, give us a first opportunity to test the analysis methods developed in this paper. Since the images have high magnification and form in regions of high-stellar density, we should not expect this system to be standardizable. The values of κ and γ for each of the iPTF16geu images have been estimated from the macro lens model published in More et al. (2017). We use the same prescription as in Section 3.2 to infer the likely smooth matter fractions at the image locations (Table 1).

In Fig. 8 we show the PDF of the change in magnitude due to microlensing for each image of iPTF16geu. These PDFs are generated assuming a time of 60 d after explosion approximately corresponding to the *Hubble Space Telescope* (HST) data analysed in More et al. (2017). More et al. (2017) noted that there is a significant discrepancy between the observed fluxes in iPTF16geu and those predicted by their lens macromodel assuming iPTF16geu is a typical SN Ia, with image A being almost 2 mag brighter than the macromodel prediction for a SN Ia. Fig. 8 shows that this discrepancy cannot be due to microlensing alone. A similar analysis by Yahalomi, Schechter & Wambsganss (2017) reaches the same conclusion using a point source, however, the tension increases for a finite sized source. We find that the discrepancies between the observed and macromodel predicted fluxes of the other three images are consistent with microlensing.

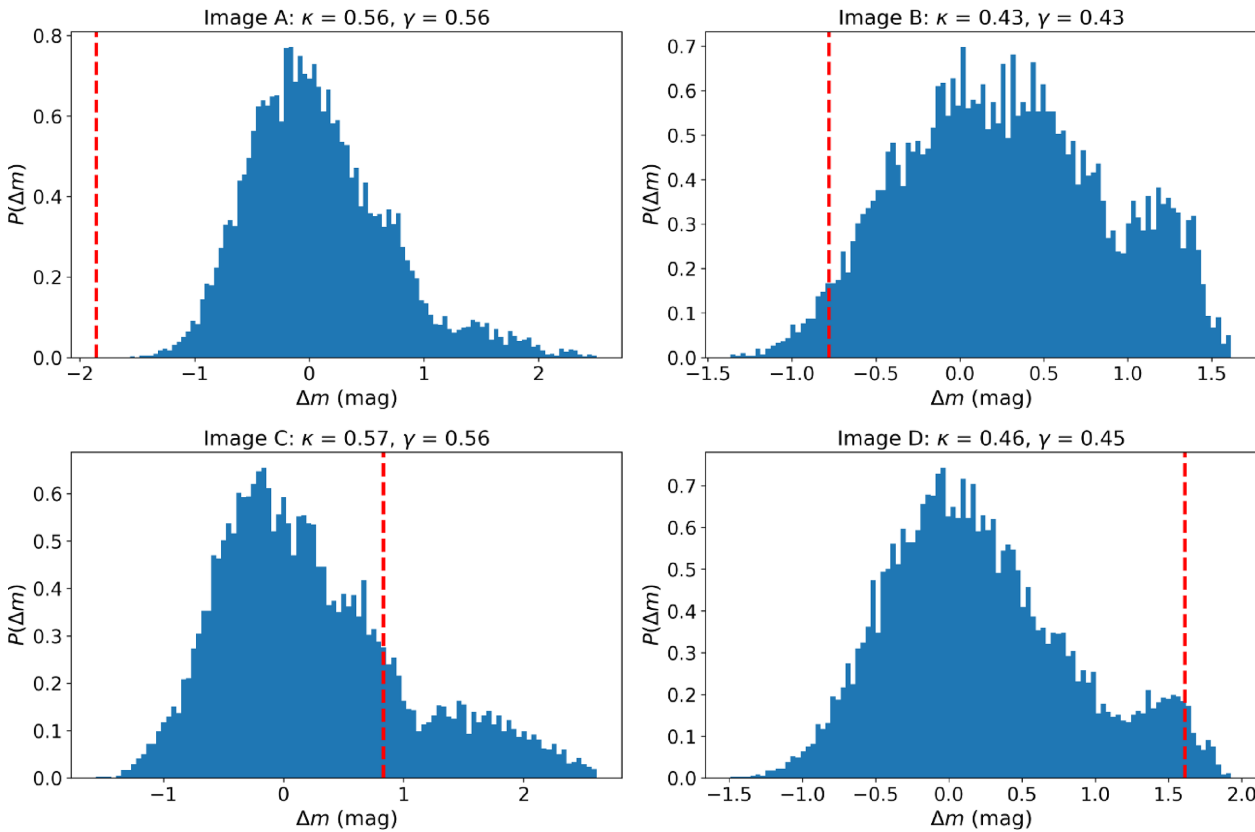


Figure 8. Histograms showing the typical magnifications for 10^4 microlensed supernovae for each image in iPTF16geu, around the time of *HST* imaging. The magnifications are in units of magnitudes and show the microlensing deviation from the smooth macromodel. The red dashed lines give the corresponding observations from Goobar et al. (2017).

If iPTF16geu has a standard Type Ia luminosity, then at least some of the disagreement in the observed and predicted fluxes must be due to deficiencies in the macromodel. The presence of a dark substructure or a stellar disc close to image A may explain this flux anomaly (Vegetti et al. 2010; Hsueh et al. 2018).

iPTF has an *r*-band discovery limit of 21st mag (Goobar et al. 2017); without the extreme magnification of image A, iPTF16geu still would have been identified as a transient by iPTF, but only marginally. The transient was only added to the spectroscopic follow-up queue when the system reached an *r*-band magnitude of 19.3 (Goobar et al. 2017). iPTF16geu would likely had not been confirmed as a GLSNe Ia without the extreme magnification of image A. The demagnification of Image D is another atypical feature of iPTF16geu. Whilst microlensing can plausibly explain the observed brightness of D, the presence of dust may also contribute to the dimming. Therefore, the micro and macrolensing of iPTF16geu are therefore unlikely to be representative of a future population of lensed SNe. However, this result does demonstrate that breaking the mass-sheet degeneracy with future lensed SNe Ia will also require a detailed reconstruction of discs and dark matter substructures in the lenses.

4 CONCLUSIONS

We have evaluated the effect of microlensing on GLSNe Ia for various image configurations, corresponding to values of the convergence κ , the shear γ , and the smooth matter fraction s , across multiple time intervals. We have found that there are regions of pa-

rameter space where the effect of microlensing is suppressed enough for the GLSNe Ia to be standardizable. Specifically, regions of low κ, γ , and high s are subject to microlensing scatter of $\sigma_{\text{ML}} \lesssim 0.15$, particularly at early times (see Fig. 4). Physically this corresponds to asymmetric configurations with at least one image located far outside the Einstein radius, which will experience the least amount of microlensing.

Combining our microlensing models with the GLSNe Ia catalogue from Goldstein et al. (2018), we predict that ~ 22 per cent of the ~ 930 GLSNe Ia to be discovered by LSST will be standardizable. From the sample of 650 GLSNe Ia, of which accurate time delays can be measured, the mass-sheet degeneracy can be broken at the 0.5 per cent level. The LSST GLSNe Ia sample will thus be robust against systematics in H_0 at the 0.5 per cent level. The assumed fraction of standardizable systems with accurate time delays may be somewhat pessimistic, since we found that standardizable GLSNe have larger Einstein radii (median 0.9 arcsec) and time delays (median 44 d), than the general population.

Our result assumes a SN Ia light profile that expands at a constant velocity of 10^4 km s $^{-1}$. Whilst simple, more complicated models can be extracted from our results by rescaling the time axis. We have not considered sources with clumpy profiles, however, since the standardizable region of Fig. 4 varies only weakly with time, our results should not be heavily influenced by the choice of source model. If the supernova profile contains any small, bright, fast moving clumps then additional scatter may be introduced. However, microlensing of such clumps would introduce rapid temporal variation in the light curve which should be easy to detect.

Whilst this paper does not focus on the IMF, we found a sharp sensitivity to the IMF for lenses with Einstein radii between 0.2 and 0.5 arcsec, assuming a lens and source with the same redshifts as in iPTF16geu. Measuring the scatter in a sample of such GLSNe Ia should trivially discriminate between the Salpeter and Chabrier fits of Auger et al. (2010).

We also applied our microlensing analysis to the GLSN Ia iPTF16geu and compared our results against the More et al. (2017) analysis, who found a strong discrepancy between the observations and their lens model, attributing the discrepancy to microlensing. Our analysis suggests that the discrepancy cannot be due to microlensing primarily (see Fig. 8) and signals potential deficiencies in the use of simple lens macromodels, as suggested by More et al. (2017).

This work shows that it is possible to infer the intrinsic luminosity for a significant sample of ~ 200 LSST GLSNe Ia, suppressing the mass-sheet degeneracy of the lens model. This will allow for accurate and precise measurements of H_0 with significantly reduced systematics through time delay cosmography, thus enabling a stringent test of the Λ CDM model of cosmology.

ACKNOWLEDGEMENTS

We thank Bob Nichol, Daniel Whalen, Daniel Thomas, Paul Schechter, Peter Nugent and the referee for constructive discussions of this paper.

We are grateful to the Royal Society for an International Exchange Grant (IE170307) which has supported our collaboration on this work.

MF is supported by the University of Portsmouth through a University Studentship. TEC is supported by a Dennis Sciama Fellowship from the University of Portsmouth. GV is supported through the Netherlands Organisation for Scientific Research VIDI grant (project number 639.043.308). DAG acknowledges support from the U.S. Department of Energy under grant DE-AC02-05CH11231, Analytical Modelling for Extreme-Scale Computing Environments. DB is supported by the Science and Technology Facilities Council consolidated grant ST/N000668/1. This work was performed on the GPU Supercomputer for Theoretical Astrophysics Research (gSTAR) national facility at Swinburne University of Technology. gSTAR is funded by Swinburne and the Australian Government's Education Investment Fund.

REFERENCES

Auger M. W., Treu T., Bolton A. S., Gavazzi R., Koopmans L. V. E., Marshall P. J., Moustakas L. A., Burles S., 2010, *ApJ*, 724, 511

- Bagherpour H., Branch D., Kantowski R., 2006, *ApJ*, 638, 946
 Betoule M. et al., 2014, *A&A*, 568, A22
 Bonvin V., Tewes M., Courbin F., Kuntzer T., Sluse D., Meylan G., 2016, *A&A*, 585, A88
 Bonvin V. et al., 2017, *MNRAS*, 465, 4914
 Collett T. E., Auger M. W., 2014, *MNRAS*, 443, 969
 Dobler G., Keeton C. R., 2006, *ApJ*, 653, 1391
 Falco E. E., Gorenstein M. V., Shapiro I. I., 1985, *ApJ*, 289, L1
 Goldstein D. A., Nugent P. E., Kasen D. N., Collett T. E., 2018, *ApJ*, 855, 22
 Goobar A. et al., 2017, *Science*, 356, 291
 Hsueh J.-W., Despali G., Vegetti S., Xu D., Fassnacht C. D., Metcalf R. B., 2018, *MNRAS*, 475, 2438
 Kayser R., Refsdal S., Stabell R., 1986, *A&A*, 166, 36
 Kolatt T. S., Bartelmann M., 1998, *MNRAS*, 296, 763
 Liao K. et al., 2015, *ApJ*, 800, 11
 LSST Science Collaboration et al., 2009, preprint ([arXiv:0912.0201](https://arxiv.org/abs/0912.0201))
 Macaulay E., Davis T. M., Scovacricchi D., Bacon D., Collett T., Nichol R. C., 2017, *MNRAS*, 467, 259
 More A., Suyu S. H., Oguri M., More S., Lee C.-H., 2017, *ApJ*, 835, L25
 Mortonson M. J., Schechter P. L., Wambsganss J., 2005, *ApJ*, 628, 594
 Oguri M., 2010, *PASJ*, 62, 1017
 Oguri M., Kawano Y., 2003, *MNRAS*, 338, L25
 Oguri M. et al., 2012, *AJ*, 143, 120
 Phillips M. M., 1993, *ApJ*, 413, L105
 Planck Collaboration et al., 2016, *A&A*, 594, A13
 Refsdal S., 1964, *MNRAS*, 128, 307
 Riess A. G. et al., 2016, *ApJ*, 826, 56
 Schneider P., Sluse D., 2014, *A&A*, 564, A103
 Shapiro I. I., 1964, *Phys. Rev. Lett.*, 13, 789
 Suyu S. H., Halkola A., 2010, *A&A*, 524, A94
 Suyu S. H. et al., 2012, *ApJ*, 750, 10
 Suyu S. H. et al., 2013, *ApJ*, 766, 70
 Tewes M. et al., 2013, *A&A*, 556, A22
 Thompson A. C., Fluke C. J., Barnes D. G., Barsdell B. R., 2010, *New A*, 15, 16
 Thompson A. C., Vernardos G., Fluke C. J., Barsdell B. R., 2014, GPU-D: Generating cosmological microlensing magnification maps, Astrophysics Source Code Library, record ascl:1403.001
 Treu T., Marshall P. J., 2016, *A&AR*, 24, 11
 Vegetti S., Koopmans L. V. E., Bolton A., Treu T., Gavazzi R., 2010, *MNRAS*, 408, 1969
 Vernardos G., Fluke C. J., 2014, *Astron. Comput.*, 6, 1
 Vernardos G., Fluke C. J., Bate N. F., Croton D., 2014, *ApJS*, 211, 16
 Vuissoz C. et al., 2008, *A&A*, 488, 481
 Wong K. C. et al., 2017, *MNRAS*, 465, 4895
 Yahalom D. A., Schechter P. L., Wambsganss J., 2017, preprint ([arXiv:1711.07919](https://arxiv.org/abs/1711.07919))

This paper has been typeset from a TeX/LaTeX file prepared by the author.